Supplemental Data. Borisjuk et al. (2013). Plant Cell 10.1105/tpc.113.111740

Supplemental Dataset 2

Appendix to Flux Balance Analysis

Methods

Flux Balance Analysis for *in-planta* developing seeds was applied using a recently published model (*bna572*) for cultured *Brassica napus* developing embryos (Hay and Schwender, 2011a, b). Minor modifications were made to the model with regards to the coefficients in the DNA and RNA assembly reactions (reactions #369, 370, see Supplemental Dataset 3A, B). In addition, the isocitrate lyase reaction was defined irreversible (see below). Individual models were derived for hypocotyl/radicle, inner cotyledon and outer cotyledon (models A, B, and C, respectively). Table 1 (main manuscript) summarizes the modeling constraints in each case. Model parameters are summarized in Table 1, and in more detail in Supplemental Dataset 3C. In each case the biomass composition, growth rate, and photon uptake flux were adjusted based on respective measurements at 32 DAF *in planta*. The growth rates were derived from the slope (algebraic derivative) of the growth curve at 32 DAF (Figure 1). Photon flux rates were based on the ambient light intensity in the growth chamber (400 µmol photons m^{-2} s^{-1}), taking into consideration measured light absorbance of pod wall, seed coat and outer cotyledons at 32 DAF. Furthermore, based on the embryo morphology (NMR-based embryo modelling dataset) the surface area of outer- and inner cotyledon and of the radicle were estimated and used to convert photon fluxes into photon uptakes per organ. In *bna572* photon uptake rates convert into photosynthetic electron transport rates. In linear electron transport the combined photochemical processes of Photosystem I and Photosystem II consume two photons (Ph_tm) per electron. The biomass composition of outer-, inner cotyledon and radicle were estimated based on NMR measurements of organ volumes, as well as water, lipid, protein and carbohydrate content. As described before (Hay and Schwender, 2011a) a generic reaction was included (ATPdrain) summarizing the effect of ATP consuming processes that would take place without growth (futile cycles, proton gradients, etc.). For each sub-model the rate of this reaction was determined separately and in the same way as in Hay and Schwender (2011a) based on a carbon balance measured for cultured dark grown embryos.

Double optimization of the three sub-models (Table 1) was performed as described before (Hay and Schwender, 2011a), each time resulting in flux variability intervals for all reactions in the network. In short, the primary optimization used minimization of substrate uptakes as the objective. The uptake rates

obtained from here were added as an additional equality constraint to the model in order to define the optimal flux space. Then a series of secondary optimizations was performed, first minimizing and then maximizing each flux in the system, resulting in flux variability intervals (fluxes see Supplemental Dataset 3A, B). Variability type nomenclature was used as previously described (Hay and Schwender, 2011a). Carbon Conversion Efficiency (CCE), the quantity of total carbon uptakes (molar percentage) that is recovered in biomass, was calculated as described before (Hay and Schwender 2011b). The relative flux through RubisCO, rate of production of 3-phosphoglyceric acid by RuBisCO (carboxylase) relative to the total net production by RuBisCO and other reactions in the network, was calculated as described before (Hay and Schwender 2011b).

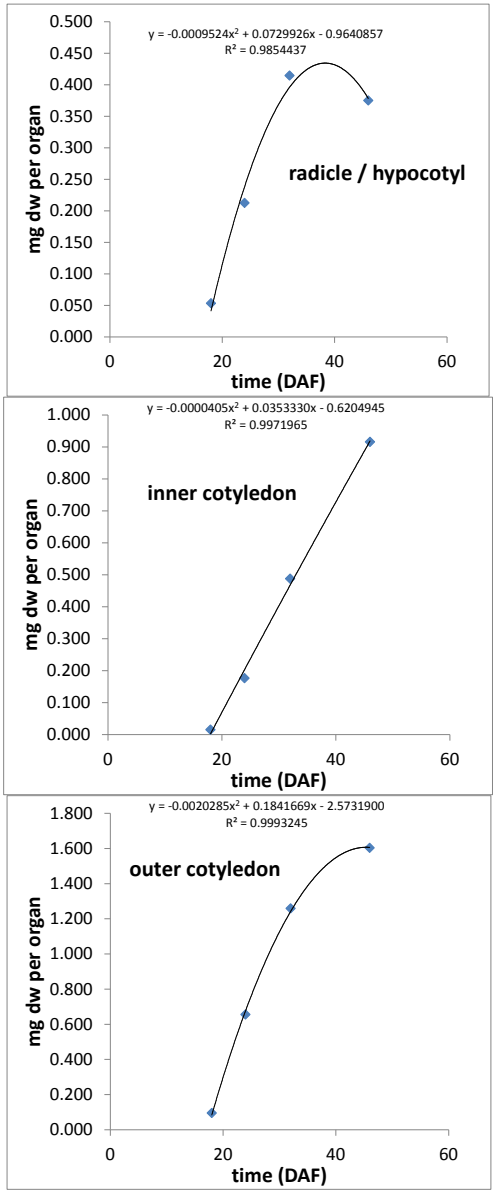

Figure 1. Dry weight increase for radicle, inner- and outer cotyledon. Based on NMR measurements. The algebraic derivative (polynom fitted curve) was used to determine growth speed at 32 DAF.

Table 1. Summarized model parameter. For comparison, the parameters as published for cultured embryos are shown. See also Supplemental Dataset 3C.

	Models, *in planta*, 32 DAF			Embryo, 10 D culture	units
Model	**A**	**B**	**C**	**PO[1]**	
Organ	**radicle / hypocotyl**	**inner cotyledon**	**outer cotyledon**	**embryo**	
Growth measurement, biomass composition, PS measurements					
Organ mass	0.3964	0.4687	1.243	10.5000	mg dw/organ
growth rate	0.0005	0.00136	0.00226	0.0725	mg dw h^{-1}
Specific growth rate	0.001261	0.002902	0.001818	0.006905	mg dw (mg dw)$^{-1}$ h^{-1}
ATPdrain (ATP_c:H2O_c::ADP_c:Pi_c)	0.014905	0.055864	0.098175	2.79	µmol h^{-1}
Light intensity reaching organ/embryo	15	1	15	50	µmol photons m^{-2} s^{-1}
total lipids (% DW)	34.8%	40.8%	42.8%	37.2%	% w / dw
total proteins (% DW)	24.2%	21.4%	21.8%	13.9%	% w / dw
DNA	0.10%	0.10%	0.10%	0.1%	% w / dw
RNA	0.10%	0.10%	0.10%	0.1%	% w / dw
starch	3.35%	3.07%	5.06%	18.1%	% w / dw
free metabolites	10.00%	10.00%	10.00%	21.2%	% w / dw
cell wall (glucose polymer)	27.42%	24.48%	20.15%	9.4%	% w / dw
fatty acid composition, mid stage					
C16 (C16H31O2)	11.49%	7.13%	6.65%	6.30%	[g/g FA]
C18:0 (C18H35O2)	2.33%	2.95%	2.47%	1.80%	[g/g FA]
C18:1 (C18H33O2)	41.73%	51.35%	47.13%	15.30%	[g/g FA]
C18:2 (C18H31O2)	31.36%	24.71%	27.88%	18.40%	[g/g FA]
C18:3 (C18H29O2)	12.12%	12.57%	14.49%	14.20%	[g/g FA]
C20:0(C20H39O2)	0.55%	0.62%	0.62%	1.00%	[g/g FA]
C20:1(C20H37O2)	0.42%	0.67%	0.76%	9.40%	[g/g FA]
C22:0(C22H43O2)	0.00%	0.00%	0.00%	1.10%	[g/g FA]
C22:1(C22H41O2)	0.00%	0.00%	0.00%	32.40%	[g/g FA]

1 Hay and Schwender 2011a,b, simulation PO (photoheterotroph, organic N); 2 Hay and Schwender 2011a,b, simulation PO (heterotroph, organic N)

Graphic presentation of network fluxes

For direct comparisons of flux rates between the models A, B and C it should be noted that the different models are simulated at largely different growth rates (Table 1), being based on estimation of *in-planta* growth rates for each individual embryo organ. To give an overview over flux distributions computed by flux variability analysis, we applied projections of the three sub-models with 572 reactions onto a smaller network with lumped reactions, representing an uncompartmentalized view of central carbon metabolism to be shown in a flux map (see Figure 6C, main text). The method highlights central carbon metabolism by showing the combined flux of parallel reactions, such as plastidic and cytosolic aldolase. In many cases this results in non-variable rates for combined fluxes, which in separate have a complex solution space defined by variable bounds.

The network projection was performed as described by Schwender et al. (2011a, b) for summed reactions and for comparison between *bna572* and fluxes obtained by ^{13}C-MFA studies. In short, the same double optimization is applied as outlined for flux variability analysis, except that in the series of secondary optimizations the objective function selects groups of reactions that are to be maximized and then subsequently minimized. For example, to determine the flux through the combined cytosolic and plastidic fructose bisphosphate aldolase, reactions 25 and 62 are identified to directly connect F16P to DHAP and G3P in the two compartments. In the secondary optimizations reactions 25 and 62 are given the coefficient -1. The negative coefficient was chosen in this case because we liked to define the summed reaction in direction F16P > DHAP + G3P:

Projected name	Objective coefficient	reaction number in bna572	Equation equation in bna572
vAldo	-1	25	1 DHAP_c + 1 G3P_c <> 1 F16P_c
vAldo	-1	62	1 DHAP_p + 1 G3P_p <> 1 F16P_p

The full definition of objective function coefficients can be found in Supplemental Dataset 3D, E.

While the above example refers to the case of the combined reaction rates of isoforms of an enzyme, other projections show the net conversion rate between two metabolites by different enzymes and in different compartiments (e.g. connections Gln > Glu; Glu > AlKG, Supplemental Dataset 3D, E).

Note that the network projection shown in Figure 6C (main text) is intended to be an interpretation of the full data (Supplemental Dataset 3A) for visualization of major sized carbon fluxes, but does not necessarily include projections of all fluxes. Therefore mass balances around metabolites in Figure 6C do not always perfectly add up.

Normalization of fluxes in graphical representation

The flux projections shown in Figure 6C (main text) are normalized relative to a sucrose uptake of 100 units (100%). This normalization allows comparison of central carbon metabolism fluxes between the models in terms of how equal amounts of sucrose uptake are distributed in the network. The normalized biomass fluxes (#368) of models A, B and C are very similar (10.87, 9.08 and 9.72, respectively). This means that normalization relative to biomass flux would result in virtually the same comparison across the models.

Changes in bna572 relative to the original publication

As mentioned above, *bna572* (Hay and Schwender, 2011a, b) was modified in this study. The coefficients of the DNA and RNA assembly reactions were slightly modified. Biomass composition, growth rate, non-growth associated ATP drain, photosynthetic ETR and light supply were adjusted for each sub-model (Table 1). We furthermore made a change in one reaction directionality constraint. In initial flux simulations of all three sub-models (A, B, C) we observed the prediction of a substantial flux via an unusual reaction sequence that leads from the glycolytic intermediate 3-phosphoglyceric acid (3-PGA) via Ser, Gly to glyoxylate and finally to the formation of isocitrate by reverse isocitrate lyase. At the same time citrate synthase was inactive so that carbon destined to oxidative degradation effectively enters the TCA cycle via glyoxylate - instead of the route via acetyl-CoA and citrate synthase (ICL_x, reaction 523). This scenario spans across the peroxisome, cytosol and mitochondria compartments and in essence constitutes an alternative cycle that replaces the condensation reaction of the TCA cycle (oxaloacetate + acetyl-CoA > citrate + CoA) by the condensation reaction of reverse isocitrate lyase “succinate + glyoxylate > isocitrate”. The *in-vivo* significance of this predicted scenario is still to be clarified. The feasibility of the flux scenario in particular hinges on the unconstrained directionality of peroxisomal isocitrate lyase (ICL_x, reaction 523), allowing the conversion of succinate + glyoxylate back to isocitrate. If this direction (condensation reaction) is disabled, the unusual reaction sequence ceases and the more conventional flux scenario is found where glycolytic flux enters the TCA cycle via pyruvate and acetyl-CoA. While the condensation reaction of Isocitrate lyase has been studied *in vitro* (Johanson et al., 1974), the enzyme is mostly known to function in the lyase direction in the context of the anaplerotic glyoxylate cycle in microorganisms and germinating seeds. Therefore we decided to present and discuss here the results of the model version with irreversibility of ICL_x, i.e. showing conventional TCA cycle activity. It turns out that all conclusions made with regards to relative RubisCO flux, Carbon Conversion Efficiency, or the relative contribution of photosynthesis to plastidial NADPH and ATP are virtually unaffected by the configuration difference in ICL_x.

Literature

Hay, J.O., and Schwender, J. (2011a). Metabolic network reconstruction and flux variability analysis of storage synthesis in developing oilseed rape (*Brassica napus* L.) embryos. *Plant J* 67**,** 526–541.

Hay, J.O., and Schwender, J. (2011b). Computational analysis of storage synthesis in developing *Brassica napus* L. (oilseed rape) embryos: flux variability analysis in relation to ^{13}C metabolic flux analysis. *Plant J* 67**,** 513–525.

Johanson, R.A., Hill, J.M., and McFadden, B.A. (1974). Isocitrate lyase from *Neurospora crassa*. Purification, kinetic mechanism, and interaction with inhibitors. Biochim Biophys Acta 364: 327-340